Superlinear Photogalvanic Effects in $(Bi_{0.3}Sb_{0.7})_2(Te_{0.1}Se_{0.9})_3$: Probing Three-Dimensional Topological Insulator Surface States at Room Temperature

S. N. Danilov,[1] L. E. Golub[ORCID],[2] T. Mayer,[1] A. Beer[ORCID],[1] S. Binder[ORCID],[1] E. Mönch,[1] J. Minár,[3]
M. Kronseder,[1] C. H. Back,[4] D. Bougeard,[1] and S. D. Ganichev[ORCID][1,5,*]

[1]*Terahertz Center, University of Regensburg, Regensburg 93040, Germany*
[2]*Ioffe Institute, St. Petersburg 194021, Russia*
[3]*New Technologies-Research Center, University of West Bohemia, Plzeň 301 00, Czech Republic*
[4]*Technical University Munich, Garching 85748, Germany*
[5]*CENTERA, Institute of High Pressure Physics PAS, Warsaw 01142, Poland*

We report on the observation of a complex nonlinear intensity dependence of the circular and linear photogalvanic currents induced by infrared radiation in compensated $(Bi_{0.3}Sb_{0.7})_2(Te_{0.1}Se_{0.9})_3$ three-dimensional topological insulators. The photocurrents are induced by direct optical transitions between topological surface and bulk states. We show that an increase in the radiation intensity results first in a highly superlinear rise in the amplitude of both types of photocurrents, whereas at higher intensities the photocurrent saturates. Our analysis of the observed nonlinearities shows that the superlinear behavior of the photocurrents is caused by heating of the electron gas, while the saturation is induced by slow relaxation of the photoexcited carriers, resulting in absorbance bleaching. The observed nonlinearities give access to the Fermi-level position with respect to the Dirac point and the energy relaxation times of Dirac fermions, providing an experimental room-temperature probe of topological surface states.

I. INTRODUCTION

Topological insulators (TIs) with low-dimensional surface states described by the massless Dirac equation have recently moved into the focus of modern research. TIs challenge fundamental physical concepts, as well as holding great potential for applications [1–5]. Recently, photocurrents excited by laser radiation in TI systems have attracted growing attention for probing the topological behavior of Dirac fermions (DFs); for a review, see Ref. [6]. In particular, photogalvanic effects (PGEs) [7–9] in TIs, including the linear [10–17] and circular [11,14,16–30] PGEs, provide important information on the electronic and spin properties of DFs and are thus highly suitable for the study of topological phenomena in various classes of TI materials [31,32]; for a review, see Ref. [16]. An important advantage of PGE phenomena is that in most cases they can be used to selectively probe the surface states of TIs even at room temperature [6,31,32]. The system properties that have been probed experimentally by PGEs are manifold: the Fermi velocity, the cyclotron masses as a function of carrier density and temperature, the orientation of surface domains in three-dimensional (3D) TIs, and the surface-state mobility. This method provides the possibility to selectively probe topological surface states (TSSs), where electronic transport experiments are often hindered by a large residual bulk charge-carrier density. In general, PGEs are caused by the redistribution of charge carriers in momentum space induced by the incident radiation. The PGE current scales with the second power of the electric field of the radiation, i.e., linearly with the radiation intensity I [7–9]. Deviations from this linearity have been observed in quantum wells [33,34] and in graphene [35], and analysis of these deviations has revealed a different way of characterizing such materials. In TIs, however, the presence of such effects has not been addressed, neither experimentally nor theoretically.

Here we demonstrate experimentally and analyze theoretically a highly nonlinear intensity dependence of both the linear and the circular photogalvanic effects. We demonstrate that the excitation of $(Bi_{1-x},Sb_x)_2(Te_{1-y},Se_y)_3$ (BSTS) with high-power midinfrared radiation results in PGE currents, which at moderate intensities exhibit a superlinear intensity dependence, followed by saturation at high I. We show that the superlinear dependence results from radiation-induced heating of the electron gas, which induces a change in the population of the initial and final states of direct optical transitions involving the topological surface states. The signal amplitude and its nonlinearity are found to be very sensitive to the position of

_____
*sergey.ganichev@physik.uni-regensburg.de

the Fermi level. Hence, the PGE represents a sensitive room-temperature probe of this important parameter. Furthermore, the photocurrent saturation, observed at very high intensities of hundreds of kW/cm^2, is shown to be caused by energy relaxation of photoexcited carriers and, consequently, yields information on the energy relaxation times of DFs.

II. SAMPLES AND METHODS

A. Samples

The TI is grown as a bilayer heterostructure [36] on $SrTiO_3$ (111) by means of molecular beam epitaxy (MBE). The heterostructures investigated here consist of one (sample A) or two (sample B and C) quintuple layers (QLs) of Bi_2Se_3 (BS) as a seed layer and 10 (sample A) or 20 QLs (sample B and C) of $(Bi_{1-x}Sb_x)_2(Te_{1-y}Se_y)_3$, with $y \approx 0.85$–0.90 to maximize the band-gap size [37], and $x \approx 0.7$–0.75 to compensate the n-type behavior of the BS seed layer. The n-type seed layer and p-type BSTS layer induce band bending in the growth direction, as shown in Fig. 1. The heterostructure is capped *in situ* by 7 nm of aluminium oxide deposited by MBE. For photogalvanic measurements, six Ti/Au contact pads are placed with rectangular symmetry around the circumference of the 4×5 mm^2 sample by optical lithography. Figure 1(b) shows a representative (here 5.6 QLs of BSTS) angle-resolved photoemission spectrum (ARPES), clearly displaying the Dirac point and the linear dispersion within the bulk band gap [36]. Other ARPES images, supported by magnetotransport on gated samples, show that the position of the Fermi energy at the top surface lies between the Dirac point (DP) and the conduction-band minimum (CBM) for BSTS thicknesses larger than approximately five QLs for the heterostructure concept presented here and this particular BSTS composition [36].

B. Methods

The photocurrents are studied by applying polarized laser radiation in the midinfrared and terahertz ranges. The sources of midinfrared radiation are two different CO_2 laser systems: a medium-power Q-switched laser with a pulse duration of 250 ns (with a repetition frequency of 160 Hz) [38,39], and a high-power pulsed transversely excited atmospheric-pressure (TEA) CO_2 laser providing 100-ns pulses with a repetition rate of 1 Hz [40,41]. These line-tunable lasers provide wavelengths in the range from 9.2 to 10.8 μm (32.6 THz $\leq f \leq$ 27.8 THz), corresponding to photon energies $\hbar\omega$ from 135 to 115 meV. The radiation is focused to a spot of about 1.5 mm diameter (for the Q-switched laser) and about 2 mm diameter (for the pulsed laser), which is much smaller than the sample size even at oblique incidence. This allows us to avoid illumination of the contacts or sample edges. The
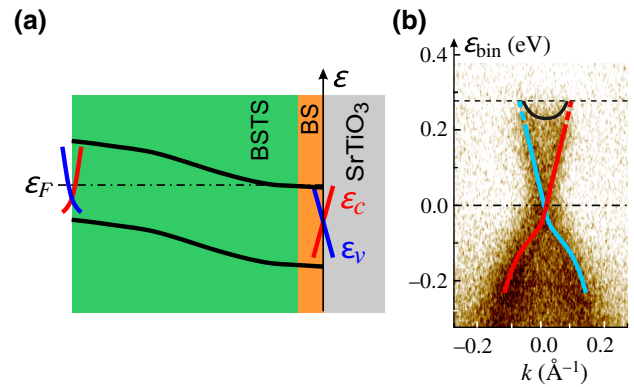

FIG. 1. Band-edge scheme of the heterostructure stack investigated. (a) The stack is built from n-type Bi_2Se_3 and a slightly p-type $(Bi_{1-x}Sb_x)_2(Te_{1-y}Se_y)_3$ ($x \sim 0.7$, $y \sim 0.9$) layer with different thicknesses: sample A, 1 QL BS + 10 QLs BSTS; samples B and C, 2 QLs BS + 20 QLs BSTS. This p-n heterostructure leads to a band-bending effect in the growth direction. In our samples [36], the Fermi energy ε_F evolves from the conduction-band minimum (CBM) at the substrate interface ($SrTiO_3$) to a midgap position at the top surface (ε_c refers to the CBM, and ε_v to the VBM). (b) ARPES at 77 K, illustrating the linear dispersion at the top surface of a heterostructure, here for a sample with the same stoichiometry ($x \sim 0.7$, $y \sim 0.9$), with 1 QL BS and 5.6 QLs BSTS, after Ref. [36].

beam positions and profiles are checked with pyroelectric cameras [42,43] or thermosensitive paper. Using different types of lasers allows us to measure photocurrents in the radiation-intensity range from $I = 0.2$ to 2 kW/cm^2 (Q-switched laser) and from 20 to 100 kW/cm^2 (TEA laser). For measurements in the terahertz spectral range, we use a line-tunable pulsed molecular laser with NH_3 as the active medium, operating at $\lambda = 90.5$, 148, and 280 μm (with $\hbar\omega$ ranging from 13.7 to 4.4 meV) [44–46]. The laser generates single pulses with a duration of about 100 ns and a repetition rate of 1 Hz, yielding a radiation intensity on the sample surface of up to 800 kW/cm^2. The peak power of the radiation is monitored, depending on the system, with photon-drag detectors [47], mercury-cadmium-telluride detectors [48], and pyroelectric power meters.

The geometry of the experiment is sketched in the inset of Fig. 2. The photocurrent is measured in unbiased structures via the voltage drop across a 600-Ω load resistor (R_L) in the experiments with the pulsed laser, and across the sample resistance in the experiments applying the Q-switched laser. The corresponding photosignal is recorded with a storage oscilloscope. Experiments are carried out at room temperature and down to 80 K, applying radiation at oblique and at normal incidence. In the measurements with oblique incident radiation, used to excite the circular photogalvanic effect, the angle of incidence Θ_0 is varied between $-40°$ and $40°$ ($\Theta_0 = 0$ corresponds to
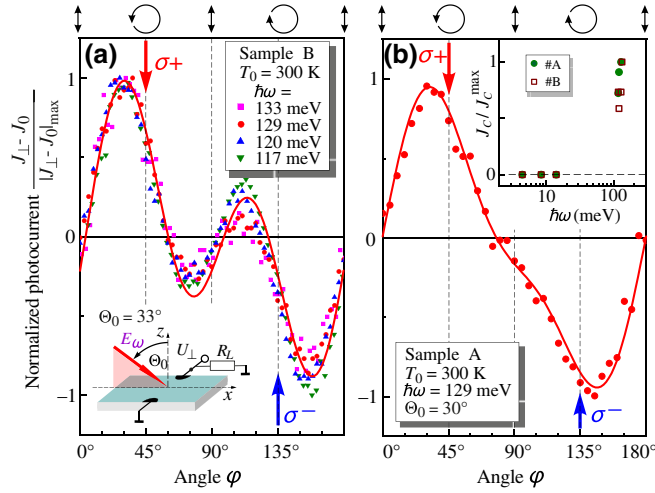
FIG. 2.   Transverse photocurrent $J_\perp$ as a function of the angle φ defining the helicity of the radiation. Note that a small polarization-independent offset J_0 is subtracted, and the current $J_\perp - J_0$ is normalized to its maximum value. The data are obtained by applying oblique-incidence radiation with an angle of incidence $\Theta = 33°$. (a),(b) Polarization dependence of the photocurrent excited in samples A and B by midinfrared radiation with different photon energies $\hbar\omega$. The solid lines are fits to Eq. (1), which corresponds to the polarization dependence of the sum of the circular PGE (CPGE) and trigonal linear PGE (LPGE) derived in the theory presented in the main text, described by Eq. (6) and the first equation in Eq. (9), respectively. The fit parameters used for the curves are (a) $J_C/J_L = 0.75$ and $\Phi = 7°$, and (b) $J_C/J_L = 3.2$ and $\Phi = 6°$. The drawings at the top illustrate the polarization states at different angles φ. The inset in (a) shows the experimental geometry. The inset in (b) presents the normalized magnitude of the circular photocurrent $J_{\text{CPGE}} = [J(\sigma^+) - J(\sigma^-)]/2$ measured for samples A and B. Note that in this inset the photoresponse to the midinfrared radiation ($\hbar\omega = 100$–130 meV) is obtained for intensities I of about 5 kW/cm^2, whereas in the terahertz range ($\hbar\omega = 4.4$–13.7 meV) substantially higher intensities of the order of 100 kW/cm^2 are applied.
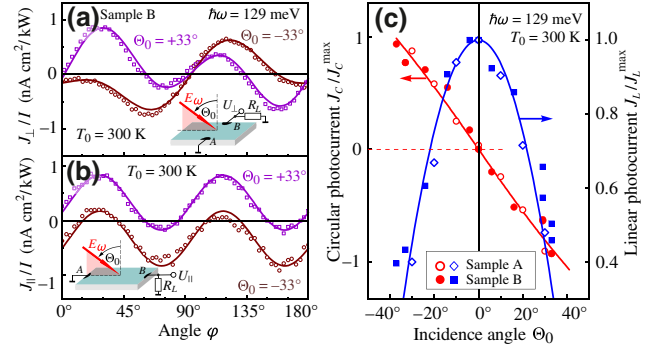

FIG. 3.   (a) Transverse photocurrent $J_\perp$ and (b) longitudinal photocurrent $J_\parallel$ as a function of the angle φ. The data are obtained for $\hbar\omega = 129$ meV, angles of incidence $\Theta_0 = \pm 33°$, and radiation intensities $I = 6.5$ kW/cm^2 (data for sample B) and 1.17 kW/cm^2 (data for sample A). In both arrangements, the signal is picked up from the contacts A and B, i.e., in the same crystallographic arrangement. The corresponding experimental setups are shown in the insets in (a),(b). The solid lines in (a) are fits after Eq. (1), which corresponds to the sum of the CPGE and the trigonal LPGE described by Eq. (6) and the first equation in Eq. (9), respectively. The fit parameters used for the curves are: for $\Theta_0 = 33°$, $J_C/J_L = 0.34/0.54$; and for $\Theta_0 = -33°$, $J_C/J_L = -0.5/0.31$. The solid lines in (b) are fits after Eq. (2), which corresponds to the first equation in Eq. (9). The fit parameter used for these curves is $J_L = 0.55$ nA. Note that in the longitudinal geometry, the CPGE vanishes. The angle Φ for all curves is $7°$. (c) Dependence of the CPGE and LPGE photocurrent contributions on the angle of incidence Θ_0 for different samples. The photocurrent is normalized to its maximum values $J_{\text{CPGE}}^{\text{max}}$ ($\Theta_0 = -40°$) and $J_{\text{LPGE}}^{\text{max}}$ ($\Theta_0 = 0$). The data are obtained for $\hbar\omega = 129$ meV, angles of incidence $\Theta_0 = \pm 33°$, and radiation intensities $I = 6.5$ kW/cm^2 (data for sample B) and 1.17 kW/cm^2 (data for sample A). The solid lines are fits after Eqs. (6) (CPGE) and (10) (LPGE). The fits are obtained assuming that the angle Θ for the radiation in the sample is equal to the angle of incidence Θ_0.

normal incidence) in the x-z or y-z plane of incidence; see the inset in Fig. 2. In our experiments, the photoresponse is probed in directions perpendicular and parallel to the incidence plane of the light, i.e., in transverse and longitudinal arrangements, respectively; see the insets in Figs. 2 and 3.

The initial polarization vector of the laser radiation is oriented along the y axis. To analyze the polarization dependence of the photocurrent, we rotate $\lambda/2$ or $\lambda/4$ plates. In the former case, the electric field vector **E** of the radiation is rotated by an azimuthal angle α with respect to the y axis, while in the latter case, apart from changes in the degree of linear polarization, we change the radiation helicity P_{circ} according to $P_{\text{circ}} = \sin 2\varphi$, where φ is the azimuth of the quarter-wave plate. Consequently, for $\varphi = 45°$ and $135°$, we obtain right-handed (σ_+) and left-handed (σ_-) circularly polarized radiation with $P_{\text{circ}} = +1$

and -1, respectively. The polarization states for some angles φ are illustrated at the top of Fig. 2.

III. RESULTS

A. Experimental study of photogalvanic effects

Figures 2 and 3(a) show the polarization dependence of the transverse photocurrent $J_\perp$, excited by oblique incident midinfrared radiation ($\Theta_0 = \pm 33°$) and measured in the direction normal to the plane of incidence. The dependence, obtained for several photon energies ranging from 117 to 133 meV, in analogy to Refs. [6,10,15], is well described by

$$J_\perp = J_C \sin 2\varphi + J_L \sin(4\varphi - 3\Phi)/2 + J_0, \quad (1)$$

where J_C, J_L, and J_0 are the magnitudes of the circular photocurrent, linear contributions, and a polarization-insensitive offset, respectively. Note that the offset J_0 is

neglected in the remainder of this paper, since it occurs only in a few of our measurements and is then found to be close to zero. The phase angle Φ, discussed below in Sec. IV, is 6° and 7° for samples A and B, respectively.

Rotating the sample by 90° and measuring now the photocurrent generated in the direction parallel to the plane of incidence (the longitudinal photocurrent, $J_\parallel$), we observe that the circular component (J_C) vanishes, and, in analogy to Ref. [10], the current follows

$$J_\parallel = J_L \sin(4\varphi - 3\Phi)/2 + J_0', \qquad (2)$$

where J_0' is a polarization-insensitive contribution. Figure 3(b) shows the data obtained for sample B for $\hbar\omega = 129$ meV and $\Theta_0 = \pm 33°$. In contrast to the transverse photocurrent $J_\perp$, in the longitudinal photocurrent ($J_\parallel$) the polarization-insensitive contribution is comparable with J_L and is odd in the angle of incidence.

Figure 3(c) presents the dependence of the amplitudes of the circular and linear contributions on the angle of incidence Θ_0. It demonstrates that the circular photocurrent is odd in the angle Θ_0 and vanishes for normal incidence, whereas the linear photocurrent is even in the angle Θ_0 and approaches its maximum at normal incidence. The data can be well fitted by $J_C \propto \sin \Theta_0$ and $J_L \propto \cos \Theta_0$.

Our analysis presented below demonstrates that the contribution to the photocurrent given by the coefficient J_L is proportional to the degree of linear polarization. Consequently, it can be excited with linearly polarized radiation. This is indeed observed. Figure 4 shows the results obtained for sample B with normally incident radiation and two in-plane directions (contact pairs AB and CD). The signals are well fitted by

$$J_{AB} = J_L \sin(2\alpha - 21°),$$
$$J_{DC} = J_L \sin(2\alpha - 21° - 45°). \qquad (3)$$

As we show below, the overall behavior of the photocurrent corresponds to that expected for the trigonal photogalvanic effect (terms proportional to the coefficients J_L) and to the circular photogalvanic effect (CPGE, the term proportional to the coefficient J_C).

B. Superlinear intensity dependence of PGE

Figures 5 and 6 show that both the circular and the linear PGE exhibit a strongly nonlinear intensity dependence: for small and moderate radiation intensities I, a superlinear increase in the photocurrent magnitude is seen for increasing I, e.g., for the room-temperature data a change of I by 1 order of magnitude results in an increase in the photocurrent by 3 orders of magnitude; see Fig. 5. At high intensities, the dependence becomes weaker and the photocurrent tends to saturate. These are surprising and central observations, since according to phenomenological and microscopic theories, photogalvanic currents
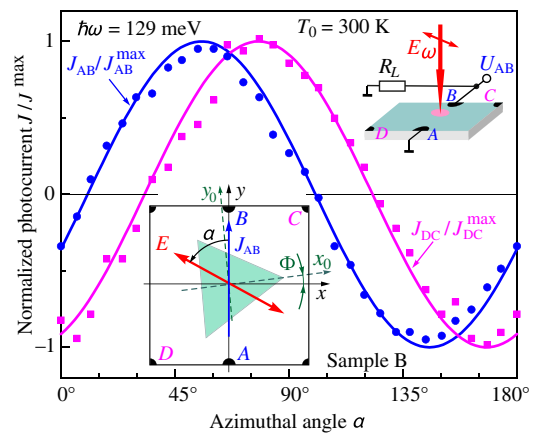

FIG. 4. Dependence of the photocurrent normalized to its maximum value. The data are obtained applying normally incident linearly polarized radiation. The photocurrent is presented for the contact pairs AB and CD. The curves are fits after Eq. (3), which corresponds to the theoretical Eq. (9) describing the trigonal PGE. The right inset shows the experimental setup. The left inset shows a sketch of the sample, the contact pairs used for the measurement, and the ac electric field vector E (double arrow). It also defines the azimuthal angle α and presents schematically the orientation of the axes along (x_0) and perpendicular to (y_0) to one of the mirror-reflection planes of the C_{3v} point group, illustrated by an equilateral triangle. Fits after Eq. (9) yield that these axes are tilted with respect to the sample edges by $\Phi = 7°$. The data are obtained for an intensity $I = 1.17$ kW/cm^2.

are expected to scale linearly with the radiation intensity. As we demonstrate in Sec. V, the observed nonlinearities can be well described by the intensity dependence of the radiation absorption.

Comparing the data for different samples, we observe that for samples B and C the magnitudes of the CPGE and LPGE photocurrents at low intensities are substantially larger than those detected in sample A; see Fig. 6(a). At the same time, the photoresponse nonlinearity detected in these samples, in particular in sample B, is significantly weaker. As long-term diffusion processes may occur in heterostructures built up from different TIs, samples B and C have nominally the same structure but are measured at different times subsequent to growth. Sample B is measured after a delay of a few months, and sample C within two weeks after growth. Stoichiometric changes become visible from the most indicative property of those compensated samples, i.e., the Fermi-level position in the BSTS layer.

When we reduce the temperature from 300 to 185 K, we observe that for sample A the signal at low intensities drastically reduces and the superlinearity is even more pronounced. Further reduction of the temperature reduces the signal at low intensity to values close to the noise level, so that the signal at low intensity falls below the sensitivity of the method, and only one point at $I \approx 8$ kW/cm^2
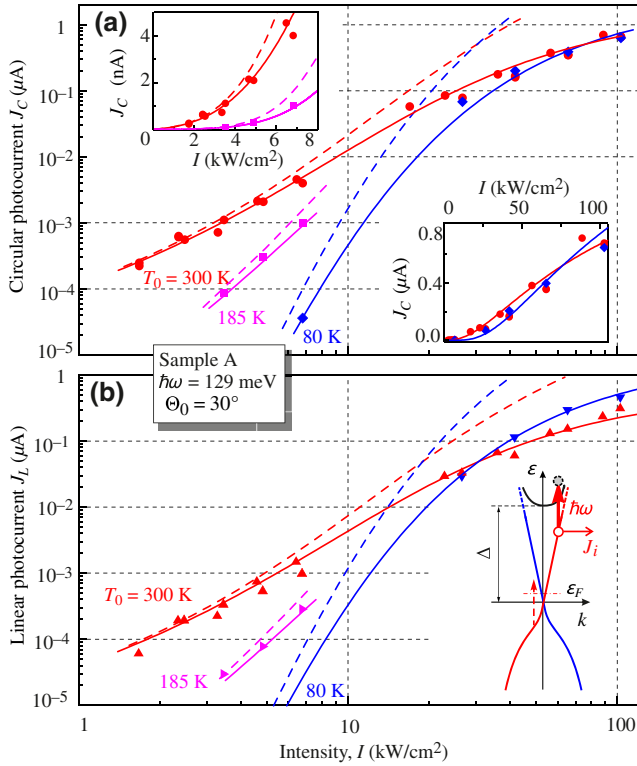
FIG. 5. Intensity dependence of the CPGE (a) and LPGE (b) contributions to the photocurrent in sample A at different temperatures. The upper and lower insets in (a) show the CPGE data on a double linear scale for the low-intensity range and the whole intensity range, respectively. The dashed lines are fits after Eqs. (17) and (18), which disregard the saturation of the photocurrent. The solid lines are fits after Eqs. (19), (20), and (21), which take saturation processes into account. The fit parameters used are $\varepsilon_i = 218$ meV, $\varepsilon_F = 8$ meV, $I_s = 50$ kW/cm^2, and $k_B \Delta T = 2I$ (kW/cm^2). The inset in (b) shows a sketch of the model of photocurrent generation due to "photoionization" of the surface states (vertical solid arrow, $\hbar\omega = 130$ meV) in samples with the Fermi energy ε_F close to the Dirac point. The spectra are extracted from the ARPES results; see Fig. 1(b). The horizontal arrow indicates the photocurrent contributions excited in the initial (J_i) state of the optical transitions. The dashed vertical arrow shows the direct optical interband transition. In the samples studied, $\Delta = 270$ meV.
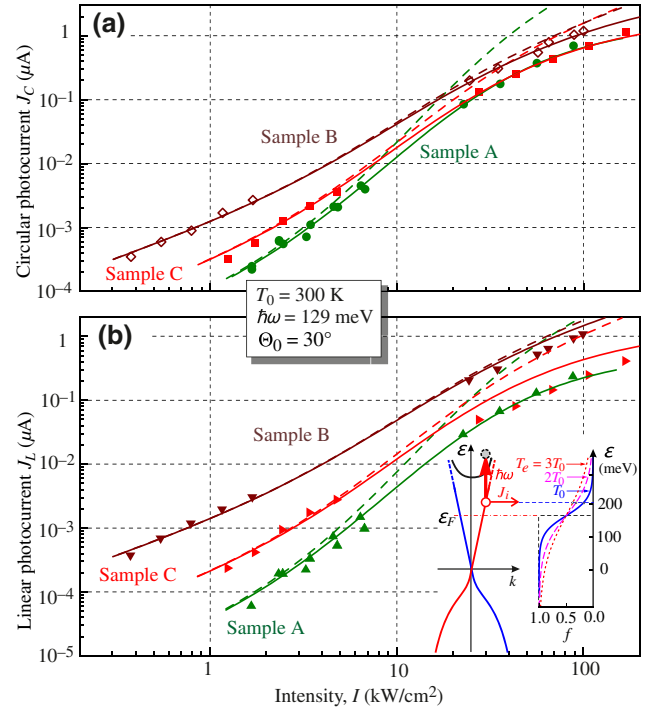
FIG. 6. Intensity dependence of the CPGE (a) and LPGE (b) contributions to the photocurrent in different samples at room temperature. The dashed lines are fits after Eqs. (17) and (18), which disregard the saturation of the photocurrent. The solid lines are fits after Eqs. (19), (20), and (21), which take saturation processes into account. The fit parameters used are $\varepsilon_i = 218$ meV, $\varepsilon_F = 8$, 122, and 80 meV, $I_s = 50$, 300, and 120 kW/cm^2 for samples A, B, and C, respectively; $k_B \Delta T = 2I$. Note the substantial differences in ε_F used for fitting data for different samples. The inset in (b) shows the model of photocurrent generation for ε_F well inside the CB, and its corresponding density of states for three different electron temperatures T_e.

is obtained with sufficient accuracy. At the same time, at very high intensities obtained by applying the TEA CO$_2$ laser, the amplitudes of the circular and linear photocurrents and their intensity dependence become comparable to those measured at room temperature; see Fig. 5.

All results described above are obtained using midinfrared radiation. Measurements with terahertz radiation reveal that at low frequencies the photocurrent vanishes [see the inset in Fig. 2(b)], even though an intensity 1 order of magnitude larger than that used in the experiments with midinfrared radiation with the TEA CO$_2$ laser is used. This observation clearly demonstrates that both the linear and

the circular PGE can not be caused by Drude absorption, for which the signal increases substantially with a decrease in frequency [$j \propto 1/(1 + \omega^2\tau^2)$ [15,16], where τ is the momentum relaxation time]. Note that the terahertz photon energies of our molecular laser used in this work are smaller by about an order of magnitude than those of the CO$_2$ laser. Combining this argument together with the fact that the observed angle-of-incidence dependence can be attributed only to the excitation of the surface layer, we conclude that the photocurrents are caused by direct optical transitions in the 3D TI topologically protected surface states, which are characterized by a linear energy dispersion, as shown in the ARPES data in Fig. 1. Note that the Rashba spin splitting, frequently discussed with respect to surface states [49,50], can not be solely responsible for the photocurrent formation, because the PGE is caused by direct transitions and the photon energies used (120–140 meV) are too large for transitions between Rashba-split subbands.

Summarizing the experimental part of this study, we demonstrate that the illumination of BSTS samples with midinfrared radiation results in linear and circular photogalvanic currents, which are caused by direct optical transitions involving topological surface states. Importantly, the observed photocurrents are characterized by a highly superlinear intensity dependence, which at high intensities tends to saturate.

IV. PHENOMENOLOGICAL THEORY

The surface of the samples studied is described by the C_{3v} point symmetry group. A phenomenological analysis yields that the PGE current density **j** is given by a sum of circular ($\mathbf{j}^{\text{circ}}$) and trigonal linear ($\mathbf{j}^{\text{tr}}$) PGE contributions [51]:

$$\mathbf{j} = \mathbf{j}^{\text{circ}} + \mathbf{j}^{\text{tr}}. \qquad (4)$$

The circular photocurrent is given by the following expression [52]:

$$\mathbf{j}^{\text{circ}} = \gamma |\mathbf{E}|^2 \hat{\mathbf{z}} \times \varkappa = \gamma i(\mathbf{E}E_z^* - \mathbf{E}^*E_z). \qquad (5)$$

Here γ is the CPGE constant, **E** is the complex amplitude of the electric field acting on the charge carriers, $\hat{\mathbf{z}}$ is the unit vector along the normal to the surface, and $\varkappa$ is the photon angular momentum, which is maximal for circularly polarized radiation. It follows from Eq. (5) that the CPGE current is perpendicular to the incidence plane and exists for oblique incidence only. For oblique incidence of elliptically polarized radiation obtained using a quarter-wave plate, the CPGE current density is given by

$$j^{\text{circ}} = \gamma E_0^2 t_p t_s \sin \Theta \sin 2\varphi. \qquad (6)$$

Here E_0 is the incident light-wave amplitude, $\sin \Theta = \sin(\Theta_0)/n_\omega$, with n_ω being the refractive index, t_p and t_s are the Fresnel amplitude transmission coefficients, and φ is the rotation angle of the $\lambda/4$ plate. We use the relation $P_{\text{circ}} = \sin 2\varphi$ for the degree of circular polarization. The CPGE, resulting in opposite directions of the transverse photocurrent for right (σ^+) and left (σ^-) circularly polarized radiation, is clearly detected in the experiment; see Figs. 2 and 3(a). The experiments also confirm the expected absence of the CPGE for the longitudinal photocurrent; see Eq. (5) and Fig. 3(b).

Equation (6) shows that the angle-of-incidence dependence of the circular photocurrent is described by $j^{\text{circ}} \propto \sin \Theta_0$. This dependence describes well the experimental results; see Fig. 3(c).

In contrast to the invariant form of the CPGE current in Eq. (5), the trigonal LPGE current $\mathbf{j}^{\text{tr}}$ is determined by the orientation of the electric vector with respect to the crystallographic axes (x_0, y_0) along and perpendicular to one of

the mirror-reflection planes of the C_{3v} point group; see the inset in Fig. 4. The current density of the trigonal LPGE is given by [10]

$$j_{x_0}^{\text{tr}} + ij_{y_0}^{\text{tr}} = \chi(E_{x_0} - iE_{y_0})^2, \qquad (7)$$

where χ is the trigonal LPGE constant. The components of the current and electric field in the coordinate system (x, y) used in the experiments are related as follows:

$$j_x^{\text{tr}} + ij_y^{\text{tr}} = \chi(E_x - iE_y)^2 e^{3i\Phi}, \qquad (8)$$

where Φ is the angle between the x and x_0 axes.

The above phenomenological Eqs. (4)–(8) demonstrate that the photocurrent perpendicular to the incidence plane is a sum of two contributions at oblique incidence, $\mathbf{j}_\perp = \mathbf{j}_\perp^{\text{tr}} + \mathbf{j}^{\text{circ}}$, while the photocurrent flowing in the incidence plane is due to the trigonal LPGE only, $\mathbf{j}_\parallel = \mathbf{j}_\parallel^{\text{tr}}$, and is maximal at normal incidence.

The trigonal LPGE is given by the in-plane components of the radiation electric field and, therefore, is proportional to the degree of linear polarization. For the photocurrent measured along lines AB and DC in Fig. 4, we have

$$j_{AB} = \chi |\mathbf{E}|^2 \sin(2\alpha - 3\Phi),$$
$$j_{DC} = \chi |\mathbf{E}|^2 \sin(2\alpha - 3\Phi - 45°). \qquad (9)$$

Here α is the angle between the linear-polarization axis and the line AB. These expressions explain the π-periodic dependence of the currents J_{AB} and J_{DC} shown in Fig. 4 and fitted by Eq. (3). The observed phase shift shows that, in the sample studied, the x_0 and y_0 directions are rotated by an angle $\Phi = 7°$ with respect to the sample edges.

For oblique incidence of elliptically polarized light obtained by using a $\lambda/4$ plate [see Figs. 2 and 3], the trigonal LPGE current is given by

$$j_\parallel^{\text{tr}} + ij_\perp^{\text{tr}} = -\frac{\chi E_0^2}{2} e^{3i\Phi} \left(\frac{3t_s^2 - t_p^2 \cos^2 \Theta}{2} \right.$$
$$\left. + \frac{t_s^2 + t_p^2 \cos^2 \Theta}{2} \cos 4\varphi - it_s t_p \cos \Theta \sin 4\varphi \right). \qquad (10)$$

Here we assume that at $\varphi = 0$ the radiation is s-polarized. For both components of the trigonal LPGE current, we obtain

$$j_{\perp,\parallel}^{\text{tr}} = \pm \frac{\chi E_0^2}{2} [A \sin(4\varphi - \varphi_0) - B], \qquad (11)$$

where φ_0, A, and B are the phase, the current amplitude, and the background signal, respectively. These are given by

$$\tan \varphi_0 = \frac{t_s^2 + t_p^2 \cos^2 \Theta}{2 t_p t_s \cos \Theta} \tan 3\Phi,$$

$$A = \sqrt{(t_p t_s \cos \Theta)^2 \cos^2 3\Phi + (t_s^2 + t_p^2 \cos^2 \Theta)^2 \sin^2 3\Phi/4},$$

$$B = \frac{3t_s^2 - t_p^2 \cos^2 \Theta}{2} \sin 3\Phi. \tag{12}$$

Note that for $\Theta_0 \leq 40°$, we obtain the angle $\varphi_0 \approx 3\Phi$ from the first equation. For small angles Φ at which $\sin 3\Phi \approx 0$ and considering $n_\omega = 1$, we obtain $A \propto \cos \Theta_0$. At normal incidence, $t_p = t_s$, and for circularly polarized radiation ($\varphi = 45°$ and $135°$), the first and second terms in the square brackets in Eq. (11) become equal to each other but have opposite signs; i.e., as expected, the LPGE vanishes.

The $\pi/2$-periodic dependence of the longitudinal photocurrent presented in Fig. 3(b) is perfectly described by the dependence $j_\parallel^{\mathrm{tr}}(\varphi)$; see Eq. (11). The dependence of the photocurrent perpendicular to the incidence plane on φ, shown in Fig. 3(a) and fitted by Eq. (1), is exactly given by the sum $j_\perp^{\mathrm{tr}}(\varphi) + j^{\mathrm{circ}}(\varphi)$. The incidence-angle dependence of the trigonal LPGE also describes the experimental results demonstrated in Fig. 3(c). We emphasize that in the experiment the angular dependence of the LPGE $j_{\mathrm{LPGE}} \propto \cos \Theta_0$ is defined by the angle of incidence Θ_0 and not by the angle Θ; see Fig. 3(b). The trigonal LPGE effects are defined by the electric field components acting on the charge carriers in the material: in-plane E fields for the trigonal LPGE and a product of in-plane and out-of plane components for the CPGE; see Eqs. (5) and (8). Consequently, in materials with large refractive indices, at oblique incidence with angles as large as $\Theta_0 = \pm 40°$, the in-plane component should remain almost unchanged, whereas the out-of-plane component should be close to zero. The fact that both photocurrents vary in the experiment with the angle of incidence shows that the photocurrent is excited in a thin surface layer in which the refraction is not yet formed.

Summarizing, we demonstrate that the detected dependence of the PGE currents is in full agreement with the phenomenological theory.

V. THEORY OF ABSORPTION OF MIDINFRARED RADIATION

The above considerations show that the photocurrent, given by Eqs. (6) and (9), is proportional to the factor χ, and to terms quadratic in the electric field amplitude yielding its polarization dependence. Consequently, the observed nonlinear intensity dependence of the photocurrent is determined solely by the nonlinearity of the polarization-independent factor χ; see, e.g., Ref. [33]. The latter is defined by the absorbance, η, which determines

the variation of the photocurrent with the radiation intensity. Therefore, we analyze in this section the absorbance spectrum at low intensity, determine the type of dominant optical transitions relevant to the experiments, and, in the next section, consider possible mechanisms for the nonlinearity of the absorption, i.e., of the photocurrent.

A. Spectral dependence of the absorbance

To estimate the value of the optical absorbance for the two relevant channels [see the inset of Fig. 5(b)], we perform band-structure calculations with the local-density approximation for Bi_2Se_3 using the linear-muffin-tin-orbital (LMTO) method [53]. We use the fully relativistic PY LMTO computer code [54], where relativistic effects are treated on the level of spin density-functional theory by solving the corresponding Dirac Hamiltonian. Self-consistent calculations of the surface are done for a slab geometry, considering 13 QLs of Bi_2Se_3 using the experimental lattice parameters. This thickness is sufficient to minimize hybridization between two TSSs and leads to a negligible gap (10^{-3} meV) at the DP. The xx component of the absorptive part of the optical conductivity tensor for finite frequencies is determined by means of the Kubo-Greenwood linear-response formalism [55,56]. In order to resolve interband transitions between the TSSs and the conduction band, we use the tetrahedron method on a very dense $64 \times 64 \times 16$ k-mesh. The calculated optical conductivity is normalized to a slab thickness of 14.318 nm to obtain the absorbance.

In Fig. 7(a), we show the calculated band structure along the path M-Γ-K in the Brillouin zone with the TSSs highlighted (green line). The calculated Fermi energy ε_{F1} (dashed line) is always at the DP. The energy denoted as ε_{F2} (blue line) is used to calculate the absorbance from transitions between the TSSs and the conduction band (CB). In Fig. 7(b), the photon-energy dependence of the absorbance, including all dipole-allowed transitions between the TSSs and CB, is shown. The maximum absorbance is about 3 in units of π times the fine-structure constant α at $\hbar\omega = 170$ meV, and is about 3 times larger than that for direct transitions between TSSs, as shown in Fig. 7(c). It is worth noting that the value of the photon energy offset [100 meV in Fig. 7(b)] depends very sensitively on the details of the band dispersion. In particular, the finite-size slab calculations limit the k-width
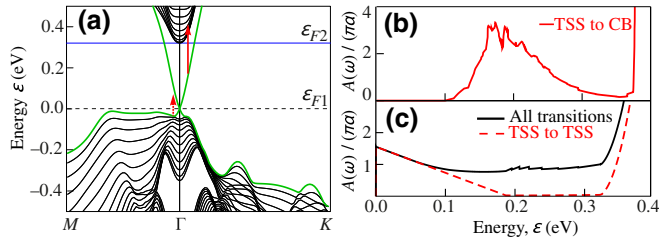
FIG. 7. (a) Electronic structure obtained from slab calculations for 13 QLs of Bi_2Se_3, with topological surface states in green and bulk states in black. (b) Low-energy optical absorbance $\sigma_{1xx}(\hbar\omega)$ between TSSs and the conduction band with respect to the shifted Fermi energy ε_{F2} (blue line) at 282 meV. (c) Total absorbance (black line) and the contribution including only direct optical transitions (dashed line) from TSSs to TSSs with the as-calculated Fermi energy ε_{F1} located at the Dirac point.

of the CB. Therefore the calculated absorbance maximum at 170 meV is in good agreement with the value of $\hbar\omega$ of 129 meV used here. Finally, in Fig. 7(c) the absorbance, including transitions between TSSs and TSSs (dashed line) as well from the valence band to the TSSs (full line), is shown. For two-dimensional materials such as graphene, with its characteristic linear p_z-orbital-based linear dispersion, the constant infrared absorbance $\pi\alpha$ has been measured [57]. However, as can be observed from Fig. 7(c) in the case of TSSs in Bi_2Se_3, we predict a linearly decreasing absorbance at low photon energies. This behavior is due to the nonlinear dispersion of the TSS close to the valence band and is connected to the strong layer dependence of the p_z and $p_{x,y}$ orbital character of the TSSs. This is reflected by the warping of the constant-energy surface [58,59].

Summarizing, in this section we show that the infrared absorbance related to the optical transition between the TSSs and CB is dominant compared with direct transitions between TSSs.

B. Optical transitions between surface and bulk states in a 3D TI

We consider the process of "photoionization" of surface states in a 3D TI where a carrier makes a transition from a surface DF state to a bulk state. The bulk-state dispersion in the conduction and valence bands can be described by [60,61]

$$E_{c,v}(\mathbf{k}) = \pm\sqrt{\Delta^2 + (A_1 k_z)^2 + (A_2 k_\parallel)^2}, \quad (13)$$

where $\mathbf{k}_\parallel$ is the projection of the wave vector onto the surface, k_z is the component normal to the surface, $A_{1,2}/\hbar$ are the anisotropic Dirac velocities, and Δ is half of the bulk band gap; see the inset in Fig. 5(b).

The surface states are localized near the surface $z = 0$ and are plane waves in the surface plane characterized

by an in-plane wave vector $\mathbf{k}_\parallel$. They have the conical dispersion $E_{s,\pm} = \pm A_2 k_\parallel$.

For the photoionization process, the energy conservation law yields

$$\hbar\omega + A_2 k_\parallel = E_c(k_\parallel, k_z), \quad (14)$$

which yields for the initial energy $\varepsilon_i = A_2 k_\parallel$

$$\varepsilon_i = \frac{\Delta^2 - (\hbar\omega)^2 + (A_1 k_z)^2}{2\hbar\omega}. \quad (15)$$

Here k_z is the projection of the wave vector of the final bulk state onto the normal to the surface. The characteristic values of k_z are in the range $0 \leq |k_z| \lesssim 1/l$, where $l = \Delta/A_1$ is the surface-state localization length. Therefore we have an estimate for the energy of the initial state,

$$\frac{\Delta^2 - (\hbar\omega)^2}{2\hbar\omega} \leq \varepsilon_i \lesssim \frac{2\Delta^2 - (\hbar\omega)^2}{2\hbar\omega}. \quad (16)$$

For $\Delta = 270$ meV and $\hbar\omega = 129$ meV, we obtain a range 218 meV $\leq \varepsilon_i \lesssim 500$ meV.

VI. DISCUSSION

A. Introductory notes

The analysis of our data in the framework of the developed phenomenological theory demonstrates that the observed photocurrents are caused by circular and trigonal linear photogalvanic effects excited in the two-dimensional surface states; see Sec. IV. Furthermore, from the spectral behavior, showing that the photocurrent is observed at high frequencies and vanishes as the frequency decreases (see Fig. 2), we can conclude that both the CPGE and the LPGE are caused by direct optical transitions, whereas mechanisms related to indirect Drude-like transitions in the experiments discussed play a negligible role. In the midinfrared range, the direct optical transitions can be caused by two mechanisms: interband transitions between DF states, and "photoionization" when one of the final or initial states lies in the three-dimensional conduction or valence band, respectively; see Sec. V A.

Both possible channels of radiation absorption may cause circular and linear PGE currents. The trigonal photogalvanic effect has been considered in the low-frequency range, where it was shown to be caused by the asymmetric scattering of carriers driven by the radiation electric field [10]. In the experiments described above, by contrast, we use high-frequency radiation, and the photocurrent is formed by direct optical transitions. Such photocurrents are always a sum of two contributions, shift and ballistic ones [7,9,52,62–64]. While the former contribution is due to shifts of the electron wave packets in real space, occurring in the process of optical absorption, the latter is caused by momentum scattering following direct

optical transitions. The theory of circular PGE in Dirac fermion systems has been developed for transitions from surface states to the continuum, considering HgTe two-dimensional and 3D TIs [21,25,26,29], and for interband transitions, considering TIs [18,20,22], graphene-based systems [65–69], and Weyl semimetals [70–77]. These results can be straightforwardly extended to the material under study and will not be discussed here.

While the trigonal LPGE photocurrent has been studied in a regime where it depends linearly on the light intensity [10,15], the nonlinear regime has not been addressed so far. Our experiments reveal that the PGE currents excited in the surface states may exhibit a highly nonlinear behavior even at moderate intensities. The photocurrent saturation observed at very high intensities is not surprising. Such behavior of the photogalvanic current has previously been detected in several different semiconductor systems and has even been applied, e.g., to determine spin relaxation times in III-V quantum wells [33,34]. The superlinearity detected at rather low intensities, however, has not been reported yet. Below, we show that both the superlinearity and the photocurrent saturation are caused by the intensity dependence of the radiation absorption. Our analysis reveals that, in all samples, the CPGE and LPGE are caused by the photoionization of surface states.

B. Analysis of the observed deviations from linearity in intensity

We begin with an analysis of the superlinearity observed in all samples excited by moderate intensities below 10 kW/cm^2; see, e.g., the top left inset in Fig. 5, presenting on a double-linear-scale plot the intensity dependence of the CPGE excited in sample A at room temperature, as well as Figs. 5 and 6, where the data for all samples are presented in a double-logarithmic presentation. While such a dependence may in principle be described in terms of two-photon absorption, our estimation shows that in the midinfrared range such transitions yield considerable contributions only for intensities many orders of magnitude larger then those used in our work [35]. At the same time, the observed superlinearity can be explained for any level of radiation intensity by considering the redistribution of carriers in energy space that results from radiation-induced electron-gas heating. The insets in Figs. 5(b) and 6(b) schematically show the generation of a PGE photocurrent caused by the "photoionization" of the surface states. As addressed above, the photocurrent is defined by the radiation absorbance η, and, as we show, its superlinearity is caused by electron-gas heating, resulting in the redistribution of carriers in energy space and an increase in η with rising intensity. For a direct optical transition, η is proportional to the difference in the occupancies of the initial and final states of the direct transition [$f_0(\varepsilon_i) - f_0(\varepsilon_f)$], where ε_i and ε_f are the energies of these states. In

the experiments discussed, the photon energies $\hbar\omega \sim 100$ meV are much higher than the thermal energy $k_B T_0$ (26 meV for experiments at room temperature and lower for low-temperature measurements). Thus, we can consider that the final states are unoccupied, which simplifies the considerations.

We begin with the results obtained on sample A, for which the position of the Fermi level $\varepsilon_F \sim 0$ is inferred from gated magnetotransport measurements [36]. In this case the initial state of the "photoionization" transition [see the inset in Fig. 5(b)] has an energy higher than the Fermi level. Thus, an increase in the electron temperature would result in an increase in the initial-state population and, consequently, in an increase in the photocurrent amplitude given by

$$j_{\mathrm{PGE}} = \frac{C I \eta_0}{1 + \exp\left[\dfrac{\varepsilon_i - \varepsilon_F}{k_B(T_0 + \Delta T)}\right]}, \qquad (17)$$

where $\Delta T = T_e - T_0$ is the intensity-dependent increase in the electron temperature T_e with respect to the lattice temperature [78], and C is a prefactor. The magnitude of the electron temperature T_e is determined by the competition between power absorption and energy loss, and can be obtained from the energy-balance equation [79]

$$\eta_0 I = n_s \frac{k_B \Delta T}{\tau_\varepsilon}. \qquad (18)$$

Here η_0 is the total absorbance involving all possible absorbance channels, considered in Sec. V A, n_s is the electron surface density, and τ_ε is the energy relaxation time of the electron gas.

Combining Eqs. (17) and (18), we obtain the intensity dependence of the PGE current. Note that in this model, the variation of the photocurrent magnitude with the radiation intensity is expected to be the same for both the CPGE and the LPGE. However, the prefactors and their variation upon change of temperature are different for these two mechanisms and reflect their microscopic details. The dashed lines in Figs. 5(a) and 5(b) show that for low intensities ($I < 10$ kW/cm^2) the experimental dependence of both the CPGE and the LPGE currents can be well fitted by the above equations. The curves obtained for different lattice temperatures show that, in agreement with the above equations, a decrease in the lattice temperature results in a higher nonlinearity. Importantly, all fits are obtained for fixed values of the Fermi level $\varepsilon_F = 8$ meV and an energy of the initial states $\varepsilon_i = 218$ meV. The latter is calculated in Sec. V B. The best fits are obtained for $k_B \Delta T$ (meV) = $2I$, where the radiation intensities are given in kW/cm^2. Consequently, for the room-temperature data set and the largest intensity of the Q-switched laser $I \approx 8$ kW/cm^2 (data points for $I < 10$ kW/cm^2), we obtain an electron temperature $T_e \sim 1.6 T_0$.

The observed superlinear intensity dependence of both photocurrents indicates that the main mechanism for their formation is based on direct transitions from the surface states to the continuum, whereas the direct interband optical transitions do not yield a measurable contribution. Indeed, in this case the initial state of the optical transition ($\varepsilon_i = -\hbar\omega/2$) is placed below the Fermi energy and the final state ($\varepsilon_f = \hbar\omega/2$) above it. Thus electron-gas heating would reduce the difference between the state occupations $[f_0(\varepsilon_i) - f_0(\varepsilon_f)]$, which should result in a sublinear intensity dependence, which contradicts the experiment.

Equations (17) and (18) also describe well the results obtained for samples B and C at room temperature. These samples are designed and grown in such a way that the Fermi levels lie closer to the CBM, above the Dirac point [36]; see the inset in Fig. 6(b). The increase in the Fermi energy results in an increase in the population of the initial state and, consequently, should lead to larger magnitudes of both photocurrents. This is indeed observed in the experiment; see Fig. 6. The best fits of the data in a low-intensity range ($I < 10$ kW/cm^2) are obtained with Fermi energies $\varepsilon_F = 122$ meV for sample B and 80 meV for sample C. Also, in these samples, a rise in the electron temperature leads to an increase in the initial-state population [see the right part of the inset in Fig. 6(b)] and, consequently, to a superlinear behavior with rising radiation intensity. A difference in the Fermi-level positions of these nominally equal samples is in line with the above-mentioned aging effect, leading in the first place to small stoichiometric changes and thereby to small changes in the Fermi level.

While Eqs. (17) and (18) describe well the observed superlinear behavior at low intensities ($I < 10$ kW/cm^2), in this form, they do not explain the observed saturation at high intensities. Saturation of the absorbance caused by direct optical transitions is in fact not surprising. Such a process, caused by slow relaxation of photoexcited carriers, has been previously detected in a great variety of semiconductor systems, including BiTe-based 3D TIs; for discussions in textbooks, see, e.g., Refs. [79,80]; for a review, see, e.g., Ref. [81]. Assuming that the absorbance saturates at high intensities as

$$\eta(I) = \frac{\eta_0}{1 + I/I_s}, \tag{19}$$

where η_0 is the low-power absorbance and I_s is the saturation intensity, we rewrite Eq. (17) in the form

$$j_{\mathrm{PGE}} = \frac{C\eta(I)I}{1 + \exp\left[\dfrac{\varepsilon_i - \varepsilon_F}{k_B(T_0 + \Delta T)}\right]}, \tag{20}$$

with ΔT defined by applying the balance equation to $\eta(I)$:

$$\eta(I)I = n_s\frac{k_B\,\Delta T}{\tau_\varepsilon}. \tag{21}$$

The corresponding fits, which are shown by solid lines in Figs. 5 and 6, describe well the data in the whole range of intensities studied, with saturation intensities $I_s = 50$–300 kW/cm^2. In general, the saturation intensity is defined by the reciprocal energy relaxation time and the absorption cross section; see, e.g., Refs. [79,80]. A detailed study of the energy relaxation time needs further experiments and is a subject of independent research.

VII. CONCLUSIONS

We demonstrate that the observed PGE results from direct transitions from the top topologically protected surface state to the bulk conduction band. Investigating the intensity dependence of the PGE, we detect a strong superlinear behavior at low and moderate radiation intensities and a sublinear behavior (saturation) at high intensities. The superlinear behavior is demonstrated to be a consequence of radiation-induced electron-gas heating, whereas the saturation results from slow energy relaxation of the photoexcited carriers. While nonlinearity of this type generally can be observed in any system, in our work we study circular and linear photogalvanic effects, which are excited selectively in the topological surface states. Our analysis of these photogalvanic effects nicely illustrates the versatility and degree of control provided by the bilayer BS/BSTS heterostructures studied, where both the versatility and the degree of control were inferred earlier from magnetotransport experiments on gated samples [36]. Indeed, here we conclude that these heterostructures provide topologically protected top surface states for which the Fermi energy lies between the Dirac point and the bulk conduction-band minimum. The position of the Fermi energy is quite precisely controlled via the thickness of the BS and BSTS layers. As conjectured for this bilayer heterostructure concept [36], in sample A the Fermi energy lies very close to the Dirac point of the surface state in the as-grown heterostructure, while in samples B and C it is found to be moved up further towards the conduction-band minimum. These conclusions, at the same time, illustrate how an analysis of the deviations from a linear dependence on intensity of the linear and circular photogalvanic effects in 3D topological insulators provides a quantitative room-temperature tool to access important materials parameters such as the position of the Fermi energy in the surface states or the energy relaxation time.

---

[1] M. Z. Hasan and C. L. Kane, Colloquium: Topological insulators, Rev. Modern Phys. **82**, 3045 (2010).

[2] Joel E. Moore, The birth of topological insulators, Nature **464**, 194 (2010).

[3] Xiao-Liang Qi, and Shou-Cheng Zhang, Topological insulators and superconductors, Rev. Modern Phys. **83**, 1057 (2011).

[4] Frank Ortmann, Stephan Roche, Sergio O. Valenzuela, eds. *Topological Insulators* (Wiley-VCH Verlag GmbH & Co. KGaA, New York, USA, 2015).

[5] David Vanderbilt, *Berry Phases in Electronic Structure Theory* (Cambridge University Press, Cambridge, UK, 2018).

[6] E. L. Ivchenko and S. D. Ganichev, in *Spin Physics in Semiconductors*, edited by Mikhail I. Dyakonov (Springer International Publishing, 2017).

[7] Boris I. Sturman and Vladimir M. Fridkin, *The Photovoltaic and Photorefractive Effects in Noncentrosymmetric Materials* (Gordon and Breach Science Publishers, London, UK, 1992).

[8] S. D. Ganichev and W. Prettl, Spin photocurrents in quantum wells, J. Phys. : Condens. Matter **15**, R935 (2003).

[9] Eougenious L. Ivchenko, *Optical Spectroskopy of Semiconductor Nanostructures* (Alpha Science, Harrow, 2005).

[10] P. Olbrich, L. E. Golub, T. Herrmann, S. N. Danilov, H. Plank, V. V. Bel'kov, G. Mussler, Ch. Weyrich, C. M. Schneider, J. Kampmeier, D. Grützmacher, L. Plucinski, M. Eschbach, and S. D. Ganichev, Room-Temperature High-Frequency Transport of Dirac Fermions in Epitaxially GrownSb2te3- andBi2te3-Based Topological Insulators, Phys. Rev. Lett. **113**, 096601 (2014).

[11] Christoph Kastl, Christoph Karnetzky, Helmut Karl, and Alexander W. Holleitner, Ultrafast helicity control of surface currents in topological insulators with near-unity fidelity, Nat. Commun. **6**, 6617 (2015).

[12] H. Plank, L. E. Golub, S. Bauer, V. V. Bel'kov, T. Herrmann, P. Olbrich, M. Eschbach, L. Plucinski, C. M. Schneider, J. Kampmeier, M. Lanius, G. Mussler, D. Grützmacher, and S. D. Ganichev, Photon drag effect in(bi1-xSbx)2te3three-dimensional topological insulators, Phys. Rev. B **93**, 125434 (2016).

[13] Lukas Braun, Gregor Mussler, Andrzej Hruban, Marcin Konczykowski, Thomas Schumann, Martin Wolf, Markus Münzenberg, Luca Perfetti, and Tobias Kampfrath, Ultrafast photocurrents at the surface of the three-dimensional topological insulator bi2se3, Nat. Commun. **7**, 13256 (2016).

[14] Kenta Kuroda, J. Reimann, K. A. Kokh, O. E. Tereshchenko, A. Kimura, J. Güdde, and U. Höfer, Ultrafast energy- and momentum-resolved surface dirac photocurrents in the topological insulator sb2te3, ' Phys. Rev. B **95**, 081103(R) (2017).

[15] H. Plank, J. Pernul, S. Gebert, S. N. Danilov, J. König-Otto, S. Winnerl, M. Lanius, J. Kampmeier, G. Mussler, I. Aguilera, D. Grützmacher, and S. D. Ganichev, Infrared/terahertz spectra of the photogalvanic effect in (bi, sb)te based three-dimensional topological insulators, Phys. Rev. Mater. **2**, 024202 (2018).

[16] Helene Plank and Sergey D. Ganichev, A review on terahertz photogalvanic spectroscopy of bi2te3- and sb2te3-based three dimensional topological insulators, Solid-State Electron **147**, 44 (2018).

[17] Y. M. Wang, J. L. Yu, X. L. Zeng, Y. H. Chen, Y Liu, S. Y. Cheng, Y. F. Lai, C. M. Yin, K. He, and Q. K. Xue, Temperature and excitation wavelength dependence of circular and linear photogalvanic effect in a three dimensional topological insulator bi2se3, J. Phys. : Condens. Matter **31**, 415702 (2019).

[18] Pavan Hosur, Circular photogalvanic effect on topological insulator surfaces: Berry-curvature-dependent response, Phys. Rev. B **83**, 035309 (2011).

[19] J. W. McIver, D. Hsieh, H. Steinberg, P. Jarillo-Herrero, and N. Gedik, Control over topological insulator photocurrents with light polarization, Nat. Nanotechnol. **7**, 96 (2011).

[20] Alexandra Junck, Gil Refael, and Felix von Oppen, Photocurrent response of topological insulator surface states, Phys. Rev. B **88**, 075144 (2013).

[21] S. N. Artemenko and V. O. Kaladzhyan, Photogalvanic effects in topological insulators, JETP Lett. **97**, 82 (2013).

[22] M. V. Entin and L. I. Magarill, Edge absorption and circular photogalvanic effect in 2d topological insulator edges, JETP Lett. **103**, 711 (2016).

[23] Ken N. Okada, Naoki Ogawa, Ryutaro Yoshimi, Atsushi Tsukazaki, Kei S. Takahashi, Masashi Kawasaki, and Yoshinori Tokura, Enhanced photogalvanic current in topological insulators via fermi energy tuning, Phys. Rev. B **93**, 081403(R) (2016).

[24] Sun Young Hamh, Soon-Hee Park, Sahng-Kyoon Jerng, Jae Ho Jeon, Seung-Hyun Chun, and Jong Seok Lee, Helicity-dependent photocurrent in a bi2se3 thin film probed by terahertz emission spectroscopy, Phys. Rev. B **94**, 161405(R) (2016).

[25] K.-M. Dantscher, D. A. Kozlov, M. T. Scherr, S. Gebert, J. Bärenfänger, M. V. Durnev, S. A. Tarasenko, V. V. Bel'kov, N. N. Mikhailov, S. A. Dvoretsky, Z. D. Kvon, J. Ziegler, D. Weiss, and S. D. Ganichev, Photogalvanic probing of helical edge channels in two-dimensional HgTe topological insulators, Phys. Rev. B **95**, 201103(R) (2017).

[26] Yu Pan, Qing-Ze Wang, Andrew L. Yeats, Timothy Pillsbury, Thomas C. Flanagan, Anthony Richardella, Haijun Zhang, David D. Awschalom, Chao-Xing Liu, and Nitin Samarth, Helicity dependent photocurrent in electrically gated (bi1-x sb x)2te3 thin films, Nat. Commun. **8**, 1037 (2017).

[27] Su-Yang Xu, Qiong Ma, Huitao Shen, Valla Fatemi, San-feng Wu, Tay-Rong Chang, Guoqing Chang, Andrés M. Mier Valdivia, Ching-Kit Chan, Quinn D. Gibson, Jiadong Zhou, Zheng Liu, Kenji Watanabe, Takashi Taniguchi, Hsin Lin, Robert J. Cava, Liang Fu, Nuh Gedik, and Pablo Jarillo-Herrero, Electrically switchable berry curvature dipole in the monolayer topological insulator WTe2, Nat. Phys. **14,** 900 (2018).

[28] Jinling Yu, Kejing Zhu, Xiaolin Zeng, Lei Chen, Yonghai Chen, Yu Liu, Chunming Yin, Shuying Cheng, Yunfeng Lai, Jin Huang, Ke He, and Qikun Xue, Helicity-dependent photocurrent of the top and bottom dirac surface states of epitaxial thin films of three-dimensional topological insulators sb2te3, Phys. Rev. B **100,** 235108 (2019).

[29] Mikhail V. Durnev and Sergey A. Tarasenko, High-frequency nonlinear transport and photogalvanic effects in 2d topological insulators, Ann. Phys. **531,** 1800418 (2019).

[30] N. Meyer, K. Geishendorf, J. Walowski, A. Thomas, and M. Münzenberg, Photocurrent measurements in topological insulator bi 2 se 3 nanowires, Appl. Phys. Lett. **116,** 172402 (2020).

[31] H. Plank, S. N. Danilov, V. V. Bel'kov, V. A. Shalygin, J. Kampmeier, M. Lanius, G. Mussler, D. Grützmacher, and S. D. Ganichev, Opto-electronic characterization of three dimensional topological insulators, J. Appl. Phys. **120,** 165301 (2016).

[32] K.-M. Dantscher, D. A. Kozlov, P. Olbrich, C. Zoth, P. Faltermeier, M. Lindner, G. V. Budkin, S. A. Tarasenko, V. V. Bel'kov, Z. D. Kvon, N. N. Mikhailov, S. A. Dvoretsky, D. Weiss, B. Jenichen, and S. D. Ganichev, Cyclotron-resonance-assisted photocurrents in surface states of a three-dimensional topological insulator based on a strained high-mobility HgTe film, Phys. Rev. B **92,** 165314 (2015).

[33] S. D. Ganichev, S. N. Danilov, V. V. Bel'kov, E. L. Ivchenko, M. Bichler, W. Wegscheider, D. Weiss, and W. Prettl, Spin-Sensitive Beaching and Monopolar Spin Orientation in Quantum Wells, Phys. Rev. Lett. **88,** 057401 (2002).

[34] Petra Schneider, J. Kainz, S. D. Ganichev, S. N. Danilov, U. Rössler, W. Wegscheider, D. Weiss, W. Prettl, V. V. Bel'kov, M. M. Glazov, L. E. Golub, and D. Schuh, Spin relaxation times of two-dimensional holes from spin sensitive bleaching of intersubband absorption, J. Appl. Phys. **96,** 420 (2004).

[35] S. Candussio, L. E. Golub, S. Bernreuter, T. Jötten, T. Rockinger, K. Watanabe, T. Taniguchi, J. Eroms, D. Weiss, and S. D. Ganichev, Nonlinear intensity dependence of edge photocurrents in graphene induced by terahertz radiation, Phys. Rev. B **104,** 155404 (2021).

[36] T. Mayer, H. Werner, F. Schmid, R. Diaz-Pardo, J. Fujii, I. Vobornik, C. H. Back, M. Kronseder, and D. Bougeard, Transport properties of band engineered p-n heterostructures of epitaxial bi2se3/(bi1-xSbx)2(te1-ySey)3 topological insulators, Phys. Rev. Mater. **5,** 014202 (2021).

[37] Byungki Ryu, Bong-Seo Kim, Ji Eun Lee, Sung-Jae Joo, Bok-Ki Min, HeeWoong Lee, Sudong Park, and Min-Wook Oh, Prediction of the band structures of bi2te3-related binary and sb/se-doped ternary thermoelectric materials, J. Korean Phys. Soc. **68,** 115 (2016).

[38] V. A. Shalygin, H. Diehl, Ch. Hoffmann, S. N. Danilov, T. Herrle, S. A. Tarasenko, D. Schuh, Ch. Gerl, W.

Wegscheider, W. Prettl, and S. D. Ganichev, Spin photocurrents and the circular photon drag effect in (110)-grown quantum well structures, JETP Lett. **84,** 570 (2007).

[39] H. Diehl, V. A. Shalygin, V. V. Bel'kov, Ch. Hoffmann, S. N. Danilov, T. Herrle, S. A. Tarasenko, D. Schuh, Ch. Gerl, W. Wegscheider, W. Prettl, and S. D. Ganichev, Spin photocurrents in (110)-grown quantum well structures, New J. Phys. **9,** 349 (2007).

[40] S. D. Ganichev, Petra Schneider, V. V. Bel'kov, E. L. Ivchenko, S. A. Tarasenko, W. Wegscheider, D. Weiss, D. Schuh, B. N. Murdin, P. J. Phillips, C. R. Pidgeon, D. G. Clarke, M. Merrick, P. Murzyn, E. V. Beregulin, and W. Prettl, Spin-galvanic effect due to optical spin orientation inn-type GaAs quantum well structures, Phys. Rev. B **68,** 081302(R) (2003).

[41] S. D. Ganichev, S. N. Danilov, V. V. Bel'kov, S. Giglberger, S. A. Tarasenko, E. L. Ivchenko, D. Weiss, W. Jantsch, F. Schäffler, D. Gruber, and W. Prettl, Pure spin currents induced by spin-dependent scattering processes in SiGe quantum well structures, Phys. Rev. B **75,** 155317 (2007).

[42] E. Ziemann, S. D. Ganichev, W. Prettl, I. N. Yassievich, and V. I. Perel, Characterization of deep impurities in semiconductors by terahertz tunneling ionization, J. Appl. Phys. **87,** 3843 (2000).

[43] P. Olbrich, J. Kamann, M. König, J. Munzert, L. Tutsch, J. Eroms, D. Weiss, Ming-Hao Liu, L. E. Golub, E. L. Ivchenko, V. V. Popov, D. V. Fateev, K. V. Mashinsky, F. Fromm, Th. Seyller, and S. D. Ganichev, Terahertz ratchet effects in graphene with a lateral superlattice, Phys. Rev. B **93,** 075422 (2016).

[44] S. D. Ganichev, W. Prettl, and P. G. Huggard, Phonon Assisted Tunnel Ionization of Deep Impurities in the Electric Field of Far-Infrared Radiation, Phys. Rev. Lett. **71,** 3882 (1993).

[45] S. D. Ganichev, I. N. Yassievich, W. Prettl, J. Diener, B. K. Meyer, and K. W. Benz, Tunneling Ionization of Autolocalized dx- Centers in Terahertz Fields, Phys. Rev. Lett. **75,** 1590 (1995).

[46] S. D. Ganichev, E. Ziemann, Th. Gleim, W. Prettl, I. N. Yassievich, V. I. Perel, I. Wilke, and E. E. Haller, Carrier Tunneling in High-Frequency Electric Fields, Phys. Rev. Lett. **80,** 2409 (1998).

[47] Sergey D. Ganichev, Ya. V. Terent'ev, and I. D. Yaroshetskii, Photon-drag photodetectors for the far-ir and submillimeter regions, Pisma Zh. Tekh. Fiz. **11,** 46 (1985).

[48] A. Rogalski, *Infrared and Terahertz Detectors* (Taylor and Francis Ltd., London, UK, 2018).

[49] Yi Zhang, Ke He, Cui-Zu Chang, Can-Li Song, Li-Li Wang, Xi Chen, Jin-Feng Jia, Zhong Fang, Xi Dai, Wen-Yu Shan, Shun-Qing Shen, Qian Niu, Xiao-Liang Qi, Shou-Cheng Zhang, Xu-Cun Ma, and Qi-Kun Xue, Crossover of the three-dimensional topological insulator bi2se3 to the two-dimensional limit, Nat. Phys. **6,** 584 (2010).

[50] P. D. C. King *et al.*, Large Tunable Rashba Spin Splitting of a Two-Dimensional Electron gas inBi2se3, Phys. Rev. Lett. **107,** 096802 (2011).

[51] Note that, generally speaking, besides these PGE currents, the phenomenological theory yields several further photocurrents for C_{3v}-symmetry systems, to which belong an LPGE currrent excited at oblique incidence, which is odd in the angle of incidence [52], as well as linear and

circular photon-drag effects [12]. An analysis of the results obtained shows, however, that in the experiments described these photocurrents do not contribute substantially.

[52] W. Weber, L. E. Golub, S. N. Danilov, J. Karch, C. Reitmaier, B. Wittmann, V. V. Bel'kov, E. L. Ivchenko, Z. D. Kvon, N. Q. Vinh, A. F. G. van der Meer, B. Murdin, and S. D. Ganichev, Quantum ratchet effects induced by terahertz radiation in GaN-based two-dimensional structures, Phys. Rev. B **77,** 245304 (2008).

[53] O. Krogh Andersen, Linear methods in band theory, Phys. Rev. B **12,** 3060 (1975).

[54] V. Antonov, B. Harmon, and A. Yaresko, *Electronic Structure and Magneto-Optical Properties of Solids* (Springer, Dordrecht, Netherlands, 2004).

[55] V. N. Antonov, A. N. Yaresko, A. Ya. Perlov, V. V. Nemoshkalenko, P. M. Oppeneer, and H. Eschrig, Magneto-optical spectroscopy of d- and f-ferromagnetic materials: Recent theoretical progress (review article), Low Temp. Phys. **25,** 387 (1999).

[56] H. Ebert, Magneto-optical effects in transition metal systems, Rep. Progr. Phys. **59,** 1665 (1996).

[57] R. R. Nair, P. Blake, A. N. Grigorenko, K. S. Novoselov, T. J. Booth, T. Stauber, N. M. R. Peres, and A. K. Geim, Fine structure constant defines visual transparency of graphene, Science **320,** 1308 (2008).

[58] Z.-H. Zhu, C. N. Veenstra, G. Levy, A. Ubaldini, P. Syers, N. P. Butch, J. Paglione, M. W. Haverkort, I. S. Elfimov, and A. Damascelli, Layer-By-Layer Entangled Spin-Orbital Texture of the Topological Surface State inBi2se3, Phys. Rev. Lett. **110,** 216401 (2013).

[59] J. Sanchez-Barriga, A. Varykhalov, J. Braun, S.-Y. Xu, N. Alidoust, O. Kornilov, J. Minar, K. Hummer, G. Springholz, G. Bauer, R. Schumann, L. V. Yashina, H. Ebert, M. Z. Hasan, and O. Rader, Photoemission of Bi2se3 with Circularly Polarized Light: Probe of Spin Polarization or Means for Spin Manipulation?, Phys. Rev. X **4,** 011046 (2014).

[60] Haijun Zhang, Chao-Xing Liu, Xiao-Liang Qi, Xi Dai, Zhong Fang, and Shou-Cheng Zhang, Topological insulators in bi2se3, bi2te3 and sb2te3 with a single dirac cone on the surface, Nat. Phys. **5,** 438 (2009).

[61] Chao-Xing Liu, Xiao-Liang Qi, Hai Jun Zhang, Xi Dai, Zhong Fang, and Shou-Cheng Zhang, Model hamiltonian for topological insulators, Phys. Rev. B **82,** 045122 (2010).

[62] L. E. Golub and E. L. Ivchenko, Shift photocurrent induced by two-quantum transitions, J. Experiment. Theoret. Phys. **112,** 152 (2011).

[63] Kun Woo Kim, Takahiro Morimoto, and Naoto Nagaosa, Shift charge and spin photocurrents in dirac surface states of topological insulator, Phys. Rev. B **95,** 035134 (2017).

[64] B. I. Sturman, Ballistic and shift currents in the bulk photovoltaic effect theory, Phys.-Uspekhi **63,** 407 (2020).

[65] Yu. Yu. Kiselev and L. E. Golub, Optical and photogalvanic properties of graphene superlattices formed by periodic strain, Phys. Rev. B **84,** 235440 (2011).

[66] E. L. Ivchenko, Photoinduced currents in graphene and carbon nanotubes, Phys. Status Solidi B **249,** 2538 (2012).

[67] M. M. Glazov and S. D. Ganichev, High frequency electric field induced nonlinear effects in graphene, Phys. Rep. **535,** 101 (2014).

[68] F. Hipolito, Thomas G. Pedersen, and Vitor M. Pereira, Nonlinear photocurrents in two-dimensional systems based on graphene and boron nitride, Phys. Rev. B **94,** 045434 (2016).

[69] S. Candussio, M. V. Durnev, S. A. Tarasenko, J. Yin, J. Keil, Y. Yang, S.-K. Son, A. Mishchenko, H. Plank, V. V. Bel'kov, S. Slizovskiy, V. Fal'ko, and S. D. Ganichev, Edge photocurrent driven by terahertz electric field in bilayer graphene, Phys. Rev. B **102,** 045406 (2020).

[70] Fernando de Juan, Adolfo G. Grushin, Takahiro Morimoto, and Joel E. Moore, Quantized circular photogalvanic effect in weyl semimetals, Nat. Commun. **8,** 15995 (2017).

[71] Ching-Kit Chan, Netanel H. Lindner, Gil Refael, and Patrick A. Lee, Photocurrents in weyl semimetals, Phys. Rev. B **95,** 041104(R) (2017).

[72] Qiong Ma, Su-Yang Xu, Ching-Kit Chan, Cheng-Long Zhang, Guoqing Chang, Yuxuan Lin, Weiwei Xie, Tomás Palacios, Hsin Lin, Shuang Jia, Patrick A. Lee, Pablo Jarillo-Herrero, and Nuh Gedik, Direct optical detection of weyl fermion chirality in a topological semimetal, Nat. Phys. **13,** 842 (2017).

[73] L. E. Golub and E. L. Ivchenko, Circular and magnetoinduced photocurrents in weyl semimetals, Phys. Rev. B **98,** 075305 (2018).

[74] Nikita V. Leppenen, Eugeniyus L. Ivchenko, and Leonid E. Golub, Nonlinear absorption and photocurrent in weyl semimetals, Phys. Status Solidi B **256,** 1900305 (2019).

[75] Zhurun Ji, Gerui Liu, Zachariah Addison, Wenjing Liu, Peng Yu, Heng Gao, Zheng Liu, Andrew M. Rappe, Charles L. Kane, Eugene J. Mele, and Ritesh Agarwal, Spatially dispersive circular photogalvanic effect in a weyl semimetal, Nat. Mater. **18,** 955 (2019).

[76] Guoqing Chang, Jia-Xin Yin, Titus Neupert, Daniel S. Sanchez, Ilya Belopolski, Songtian S. Zhang, Tyler A. Cochran, Zijiã Chéng, Ming-Chien Hsu, Shin-Ming Huang, Biao Lian, Su-Yang Xu, Hsin Lin, and M. Zahid Hasan, Unconventional Photocurrents from Surface Fermi Arcs in Topological Chiral Semimetals, Phys. Rev. Lett. **124,** 166404 (2020).

[77] Dylan Rees, Kaustuv Manna, Baozhu Lu, Takahiro Morimoto, Horst Borrmann, Claudia Felser, J. E. Moore, Darius H. Torchinsky, and J. Orenstein, Helicity-dependent photocurrents in the chiral weyl semimetal RhSi, Sci. Adv. **6,** eaba0509 (2020).

[78] We assume that the electron-electron collision time is much shorter than the energy relaxation time. Under this condition, the electron gas establishes a temperature T_e, which is different from the temperature of the lattice.

[79] Sergey Ganichev and Willi Prettl, *Intense Terahertz Excitation of Semiconductors* (Oxford University Press, Oxford, UK, 2005).

[80] Bahaa E. A. Saleh and Malvin Carl Teich, *Fundamentals of Photonics* (John Wiley and Sons Ltd., New York, USA, 2019).

[81] Anton Autere, Henri Jussila, Yunyun Dai, Yadong Wang, Harri Lipsanen, and Zhipei Sun, Nonlinear optics with 2d layered materials, Adv. Mater. **30,** 1705963 (2018).